# Super-resolution mapping of coastline with remotely sensed data and geostatistics

**ZHANG Yang, CHEN Shen-liang**

*State Key Laboratory of Estuarine and Coastal Research, East China Normal University, Shanghai* 200062, *China*

**Abstract:** The soft classification results of coarse-resolution data and the coarse & fine resolution variograms were derived, using the Landsat satellite data of the modern Yellow River Delta coast. Treating the fine-resolution indicator vriogram as the prior model of spatial structure of the study area, the super-resolution images of land & ocean class were generated using data exploratory analysis, indicator cokriging (ICK), and sequential indicator co-simulation (SIcS) techniques. Then the spatial distribution features of the coastline were extracted by the contouring method. Taken human interpretation output as the benchmark, the coastline mapping results derived from geostatistics showed better quality than that derived from traditional hard-classification methods. Super-resolution mapping techniques based on geostatistics can properly illustrate spatial distribution of coastline at fine scale; meanwhile maintain the class fraction values and the spatial structures of the original coarse-resolution data. By the form of super-resolution mapping of coastline, the potential of the geostatistical techniques in integrating multi-source and multi-scale spatial information has been demonstrated.

**Key words:** remotely sensed data, geostatistics, coastline, super-resolution mapping, the modern Yellow River Delta

**CLC number:** TP79/P237 **Document code:** A

**Citation format:** Zhang Y, Chen S L. 2010. Super-resolution mapping of coastline with remotely sensed data and geostatistics. *Journal of Remote Sensing*. 14(1): 148—164

## 1 INTRODUCTION

Coastline is the boundary between land and ocean. Largely due to the dynamic nature of water levels at the coastal boundary, coastline position changes continuously through time (Boak & Turner, 2005). Detecting coastline position and its variability is the elementary content of coastal monitoring and management. Because of the particularity of coastal environment and its dynamic nature, traditional field surveying approach is labor intensive, time consuming, and sometimes is restricted by the difficulty of access. Therefore, remote sensing technology, which is considered as a rapid and cost-effective data collection method, has been widely applied to coastal information extraction and monitoring work (Zhang *et al.*, 2009). According to the specifications of Chinese Nautical Charts (GB12319-1998) and Chinese Topographic Maps (GB/T5791-93), the standard definition of coastline is the mean high water boundary for dividing land and ocean. However, this kind of boundary does not exist in reality; so waterline is used to indicate the boundary between land and ocean instead. Waterline is more recognizable and with the highest continuity on remote sensing images. In general, near-infrared (NIR, e.g. Landsat TM 4) and short wavelength-infrared (SWIR, e.g. Landsat TM 5) bands are effective in detecting sandy coast or clear water boundary (Manavalan *et al.*, 1993; Frazier & Page, 2000). In tidal flat zone, thermal-infrared (TIR) band is the most sensitive band to the location of waterline (Ryu *et al.*, 2002; Shen *et al.*, 2008), but the spatial resolution of TIR bands are often not high enough (e.g. 120m/60m in Landsat TM/ETM+ and 90m in EOS-Terra ASTER). Moreover, the earth surface observed through the instaneous field of view (IFOV) of these sensors at such moderate resolution may be very heterogeneous, leading to spectral confusion. Therefore, the accuracy of coastline mapping is heavily limited (Malthus & Mumby, 2003).

The main solution to spectral confusion issue is spectral unmixing, which estimates the proportions of each class fraction in the mixed pixel using a variety of fuzzy or soft classification methods (Foody, 1996). This approach can provide higher and more suitable class fraction information than pixel-based hard classification, but it cannot locate these constituent classes (Atkinson, 1997). Aimed at this issue, many methods were developed in recent years for locating spatial distribution of each class fraction at a subpixel scale, and have been successfully applied to land use\land cover mapping (Ta-

**Received**: 2008-10-20; **Accepted**: 2009-05-31

**Foundation**: National marine public sector funding for scientific research and special projects (No. 200805063); Scientific Research Project of State Key lab of Estuary & Coastal Research (SKLEC) (No. 2008 KYYW06).

**First author biography**: ZHANG Yang (1975— ), male, post-doctor, graduated from Institute of Geographic Sciences and Natural Resources Research, Chinese Academy of Sciences, majoring on Cartography and Geographical Information System in 2007. He at present engaged in coastal remote sensing and GIS application research. E-mail: zhangyang2907@163.com

tem *et al.*, 2003; Boucher & Kyriakidis, 2006). The main purpose of these methods is to map the theme of interest at a scale that is finer than the data set from which it was derived. They are commonly referred to as super-resolution mapping methods. The potential of super-resolution technology in coastline mapping has been demonstrated from simulated scene experiments (Foody *et al.*, 2005; Muslim *et al.*, 2007). In general, super-resolution mapping can be formulated within an inverse problem theory perspective, which reconstructs a fine-spatial resolution map of class labels from a set of coarse-spatial resolution class fractions (Boucher *et al.*, 2008). Because this inverse problem is under-determined, prior information (e.g. a prior model of spatial structure at fine scale) is needed to limit the under-determination and constrain the spatial patterns of class labels to be generated at fine resolution. The prior models can be based on maximum spatial continuity assumption (Atkinson *et al.*, 1997; Verhoeye & De Wulf, 2002), or variogram models in geostatistical analysis (Atkinson, 2004; Boucher & Kyriakidis, 2006). In this paper, a preliminary experiment of super-resolution mapping of coastline with remotely sensed data and geostatistics was presented. The pixel values of real-scene remotely sensed data were considered as regionalized variables, and original data and prior model of spatial structure at fine scale were integrated into land-sea spectral classification of target imagery.

## 2 MATERIAL AND METHODS

### 2.1 Study area and data description

The modern Yellow River Delta, located in Shandong province of China, is one of regions where spatial-temporal changes between land and ocean are most vibrant. It was developed since the Yellow River breached at Tongwaxiang, Henan Province, and entered the Bohai Sea in 1855. Due to the strong effects of river and ocean dynamics, the modern Yellow River Delta coast has been eroded and accreted alternately. According to the coastal erosion/accretion pattern in recent years, the coastal characteristics of this area can be divided into weak erosion, strong erosion and strong accretion (Chen *et al.*, 2004). The study area in this paper are the artificial coast located at the Yellow River Harbor (A in Fig. 1), and the silty coast located at the Yellow River Estuary (B in Fig. 1). There was little changes happened on the coast at the harbor due to protection of the defense bank; meanwhile the coast at the estuary changed rapidly due to river and ocean dynamics effects.

According to Garrigues *et al.* (2006), the remotely sensed data used in geostatistical analysis requires several assumptions, including (1) co-registration errors between the spectral bands are small enough to assume that spatial supports of remotely sensed data are identical; (2) the image extent is large with respect to the spatial features of interest; (3) the radiometrics measurement errors are assumed to be small relative to the surface variations; and (4) the effects of spatial variations at

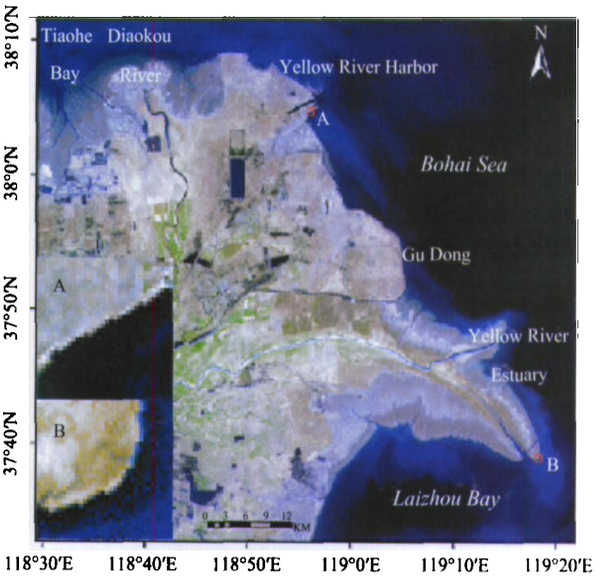


Fig. 1 Location of the study area with RGB composite map from Landsat-7 ETM+, 2000

scale smaller than the sampling step of the sensor can be neglected. The Landsat-7 ETM+ thermal-infrared band 6 data acquired on May 2nd, 2000 (spatial resolution is 60m, and pixel size is 57m) was used as coarse-resolution data source for coastline mapping. Thermal-infrared bands can be linked directly to surface cover, and their measure system is different from that of reflective bands. Thermal-bands may be used in association with other TM bands for monitoring or recording information of the same pixels. When actual field verification is not feasible, this combination is timely and cost-effective (Southworth, 2004). The panchromatic band 8 data (spatial resolution is 15m, and pixel size is 14.25m) were used as data source for prior information at fine scale, in order to ensure a unified data imaging environment, and diminish the co-registration errors and time errors between mapping data and reference data. Therefore, assumption (1) was satisfied. Table 1 is the Landsat data description used in the study.

### 2.2 Methodology

The methodology used in this study is based on the technical framework of indicator geostatistics proposed by Boucher and Kyriakidis (2006), and incorporated with spectral characteristics of land and ocean on remote sensing images. It is summarized as follows:

*2.2.1 Class indicator and fraction*

Let c(v) denote the unknown class (seawater or land) at a fine resolution pixel $v=v(\boldsymbol{u})$, where $\boldsymbol{u}$ is the coordinate vector of its centroid and the pixel area is denoted as $|v|$. The set of all unknown class labels constitutes a $(M\times1)$ vector $\boldsymbol{c}=[c(v_m), m=1,...,M]^T$, where $M$ denotes the number of fine resolution pixels. The presence or absence of the seawater class label at pixel $v$ is coded by a binary class indicator $i(v)$, defined as $i(v)=1$. If $c(v)$ is seawater, zero if not. The set of all indicators for seawater class can be arranged in a $(M\times1)$ vector $\boldsymbol{i}=[i(v_m),$

**Table 1 Descriptive statistics of the pixel values of the Landsat images used in the study**

| Data | Pixel | Minimum | Maximum | Average | Median | Variance | Kurtosis | Skewness |
|---|---|---|---|---|---|---|---|---|
| Band6 (A) | 16×16 | 125 | 173 | 146.70 | 143 | 354.58 | 1.15 | 0.09 |
| Band8 (A) | 64×64 | 21 | 103 | 59.78 | 53 | 256.32 | 1.46 | 0.19 |
| Band6 (B) | 16×16 | 121 | 165 | 142.65 | 143 | 301.37 | 1.15 | 0.03 |
| Band8 (B) | 64×64 | 36 | 83 | 56.92 | 57 | 82.61 | 2.02 | 0.17 |

$m=1,...,M]^T$. Let $a(V)$ denote the fraction of seawater class at a coarse resolution pixel $V=V(\boldsymbol{s})$, where $\boldsymbol{s}$ is the coordinate vector of it centroid and the pixel area is denoted as $|V|$. The set of all fraction values for seawater class constitutes $a$ ($N\times1$) vector $\boldsymbol{a}=[a(V_n),\ n=1,...,N]^T$, where $N$ denotes the number of coarse resolution pixels. $F=|V|/|v|=M/N>>1$ denotes the resolution ratio between coarse and fine resolution images. Because both images are co-registered, there are $F$ fine resolution pixels $\{v_m,\ m=1,...,\ F\}$ in any coarse resolution pixel $V$. The objective of super resolution mapping can be formulated as the task of finding the unknown class label vector $\boldsymbol{c}$ from the seawater class fraction vector $\boldsymbol{a}$ (Boucher & Kyriakidis, 2006).

*2.2.2 Indicator variogram*

The spatial distribution of seawater class at fine resolution can be characterized by its stationary proportion and its spatial structure. Let $\delta$ denote the stationary proportion of seawater class. In the coarse resolution pixel $V_n$, the seawater class fraction value $\boldsymbol{a}(V_n)$ is defined as the average of the seawater class indicators at the $F$ fine pixels within $V_n$:

$$a(V_n)=\frac{1}{F}\sum_{m=1}^{F} i(v_m), v_m\in V_n \tag{1}$$

The mean $\bar{a}$ of the seawater class fraction values equals to the corresponding proportion $\delta$ of the seawater class indicators:

$$\begin{aligned}\bar{a}&=\frac{1}{N}\sum_{n=1}^{N}a(V_n)=\frac{1}{N}\sum_{n=1}^{N}[\frac{1}{F}\sum_{m=1}^{F}i(v_m)]\\&=\frac{1}{M}\sum_{m=1}^{M}i(v_m)=\delta\end{aligned} \tag{2}$$

The indicator variogram $2\gamma^v(\boldsymbol{h})$ denotes the joint probability of any two fine pixels separated by vector $\boldsymbol{h}$, superscript $v$ denotes that $2\gamma^v(\boldsymbol{h})$ pertains to $v$ fine resolution pixels (Carle & Fogg, 1996). $2\gamma^v(\boldsymbol{h}_{mm'})=2\gamma^v(\boldsymbol{u}_m-\boldsymbol{u}_{m'})$ denotes the indicator variogram between two unknown fine pixels $v_m$ and $v_{m'}$, whose respective centroids $\boldsymbol{u}_m$ and $\boldsymbol{u}_{m'}$ are separated by $\boldsymbol{h}_{mm'}=\boldsymbol{u}_m-\boldsymbol{u}_{m'}$. Let $2\gamma^v(\boldsymbol{h};\ \boldsymbol{\theta})$ denote the fine resolution variogram of seawater class, with $\boldsymbol{\theta}$ being a vector of model parameters. The fine-to-coarse resolution variogram between the seawater class indicator $i(v_m)$ at the fine pixel $v_m$ and the seawater class fraction $\boldsymbol{a}(V_n)$ at the coarse pixel $V_n$ is a function of the separation vector $\boldsymbol{h}_{mn}$ between the two pixel centroids $\boldsymbol{u}_m$ and $\boldsymbol{s}_n$, i.e. :

$$2\gamma(v_m;V_n)=2\gamma(v(\boldsymbol{u}_m);V(\boldsymbol{s}_n))=2\gamma^{vV}(\boldsymbol{u}_m-\boldsymbol{s}_n)=2\gamma^{vV}(\boldsymbol{h}_{mn}),$$

with superscript $vV$ indicating that $2\gamma^V(\boldsymbol{h}_{mn})$ is a cross-resolution variogram between $v$ fine pixels and $V$ coarse pixels. The variogram between the seawater class fractions at two coarse pixels $V_n$ and $V_{n'}$ is a function of separation vector $\boldsymbol{h}_{nn'}$ between the two pixel centroids $\boldsymbol{s}_n$ and $\boldsymbol{s}_{n'}$, i.e.:

$$2\gamma(V_n;V_{n'})=2\gamma(V(\boldsymbol{s}_n);V(\boldsymbol{s}_{n'}))=2\gamma^V(\boldsymbol{s}_n-\boldsymbol{s}_{n'})=2\gamma^V(\boldsymbol{h}_{nn'}),$$

with superscript $V$ indicating that $2\gamma^V(\boldsymbol{h}_{mn'})$ is a coarse resolution variogram between $V$ coarse pixels (Boucher & Kyriakidis, 2006). The variogram for fine resolution seawater class indicators, the fine-to-coarse variograms between seawater class indicators and corresponding coarse fractions, and the variogram between coarse seawater class fractions are used to estimate the probability of seawater class occurrence at any fine resolution pixel (Journel & Huijbregts, 1978; Atkinson & Curran, 1995).

*2.2.3 Indicator coKriging (ICK)*

Based on the coarse fraction data $\boldsymbol{a}(V)$, ICK can yield an approximation $\hat{p}(v)$ to the true probability $p(v)=\text{Prob}\{I(v)=1|\boldsymbol{a}\}$ of seawater class occurrence at any fine resolution pixel $v$ (Journel, 1983; Goovaerts, 1997). Because the seawater class proportions are assumed known, the simple ICK is adopted to estimate the fine pixel $v_m$:

$$\hat{p}(v_m)=\eta(v_m)^T\boldsymbol{a}+\delta[1-\eta(v_m)^T\boldsymbol{1}_N] \tag{3}$$

where, $\eta(v_m)=[\eta_n(v_m),n=1,...,N]^T$ denotes the ($N\times1$) vector of the weights assigned to $N$ seawater class fractions; $\boldsymbol{1}_N$ denotes ($N\times1$) vector of ones; The known seawater class proportion $\delta$ is considered as the weight of the complement to $\eta(v_m)$ $\boldsymbol{1}_N$. The ICK weight $\eta(v_m)$ for seawater class is obtained by solving the following equation:

$$\Gamma^{VV}\eta(v_m)=\gamma^{vV}(v_m) \tag{4}$$

where, $\Gamma^{VV}=[2\gamma^V(\boldsymbol{h}_{nn'}),n=1,...,N,n'=1,...,N]$ is a ($N\times N$) matrix of the fraction variogram values between all pairs of the coarse pixels; $\gamma^{vV}(v_m)=[2\gamma^{vV}(\boldsymbol{h}_{mn}),n=1,...,N]^T$ denotes a ($N\times1$) vector of the variogram values between the uninformed fine pixel $v_m$ and the $N$ coarse pixels.

*2.2.4 Sequential Indicator co-Simulation (SIcS)*

SIcS algorithm generates synthetic maps of land and seawater classes, based on a sample set of known categories and a set of indicator variogram models (Journel & Alabert, 1989; Goovaerts, 1997). The multivariate probability distribution function $\int(i|\boldsymbol{a})$ of $M$ indicator Random Variables (RV) $\{I(v_m),\ m=1,...,M\}$ is decomposited into a sequence of $M$ univariate conditional probabilities by SIcS method as follows:

$$\int(i\,|\,a) = \text{Prob}\{I(v_1) = i(v_1),\ldots,I(v_M) = i(v_M)\,|\,a\} = \prod_{m=1}^{M} \text{Prob}\{I(v_m) = 1\,|\,i^{m-1}, a\} \quad (5)$$

where, $\text{Prob}\{I(v_m)=1\,|\,i^{m-1},a\}$ is the conditional cumulative distribution function (CCDF) of the indicator RV $I(v_m)$; the $m-1$ previously simulated indicator values of seawater class are stored in a $((m-1)\times 1)$ vector $i^{m-1}=[i(v_{m'}),m'=1,\ldots,m-1]^{\mathrm{T}}$; The original data vector $a$ includes the $N$ coarse resolution fractions of seawater class. The simulated random path is built by a sequence of the $M$ fine resolution pixels, and thus determines the order of the decomposition given in Eq. (5). At any fine pixel $v_m$ along that path, a simulated class label $c(v_m)$ is generated from the corresponding ICK-derived conditional probability at that pixel. The associated simulated indicators $i(v_m)$ constrain all subsequent univariate conditional probabilities and all subsequent simulated class labels generated from such probabilities. A simulated realization of the class labels generated from repeating the above steps at all $M$ fine resolution pixels is denoted as $c=[c(v_m),\ m=1,\ldots,M]^{\mathrm{T}}$. The new simulated realization of the class labels can be created from repeating various random paths (Goovaerts, 1997).

## 3 STUDY RESULTS

### 3.1 Soft classification

For the coastline at the Yellow River Harbor (A in Fig. 1), classification-based methodology with coarse resolution imagery was adopted, categorized as land and seawater class. The coastline on the coarse resolution imagery was predicted by traditional supervised classification, and regarded as the comparison data. Soft classification on the coarse imagery was implemented with fuzzy set membership functions provided by IDRISI software, whose result was the predicted values of seawater class fraction in each pixel (Fig. 2(a)). These fuzzy membership values denoted the proportion of the pixel area that was covered with seawater, while the reminder was ascribed to land. Because the output on pure seawater pixels that did not contain coastline information commonly had a high, but not full 1.0 membership to seawater, these memberships were rescaled to 1.0 to remove their potentially problematic influences. Correspondingly, the output on pure land pixels that did not contain coastline information was rescaled to 0. The rescaled output was considered as the seawater class fraction data of the coarse resolution imagery. The output accuracy was assessed through a comparison of the predicted coverage of seawater class with that derived from the reference data (Fig. 2(b)). The predicted coverage and the reference data were highly correlated ($R^2$=0.9126), indicating that the soft classification result was an appropriate base for super-resolution mapping.

### 3.2 Data exploratory analysis

The first important step in all geostatistical analysis is to establish correct variable data and make sure that their properties are stationary over the domain of study (Gringarten & Deutsch, 2001). If variable data are skew-distributed or have outliers, the experimental variogram will be influenced and thus show distribution peculiarities. The indicator geostatistics used in this study can remove this data sensitivity to outliers, and present a distribution-free characteristic (Carr *et al.*, 1985). For each pixel observation value $Z(x_i)$ $i$=1,2,$\cdots$,$n$, the corresponding indicator function is defined as the following equation:

$$I(x) = \begin{cases} 1, x \leqslant v_c \\ 0, x > v_c \end{cases} \quad (6)$$

the threshold value $V_C$ was determined from the variation range of pixel values of the fine resolution imagery. Fig.3 (a) was the indicator-transformed experimental variogram based on the original data.

It can be seen from Fig.1 that the spatial structure of land and seawater on the image was beyond the image extent. In Fig. 3 (a), the indicator variogram curve kept increasing above the maximum theoretical sill value 0.25, indicating an obvi-

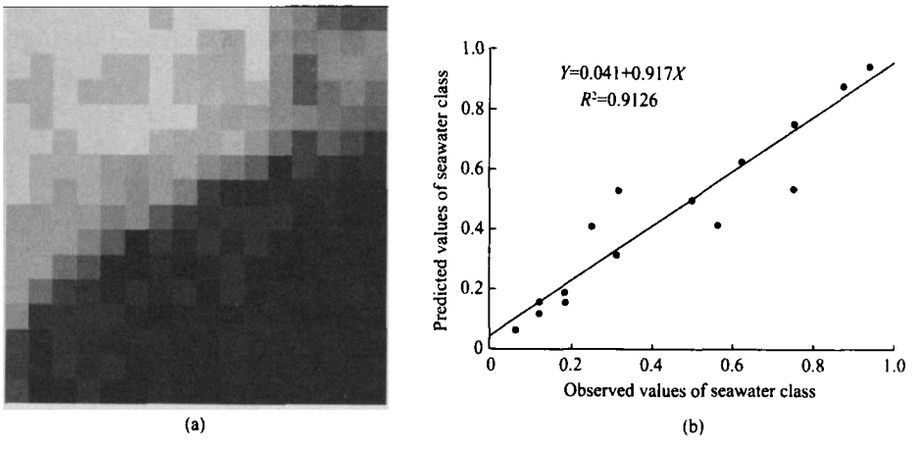


Fig.2 (a) Soft classification derived from fuzzy set of the study area coarse-resolution image. The grayscale indicates the degree of membership to the water class that was considered as an estimate of the proportional coverage of water (white=complete land cover, black=complete water cover); (b) Relationship between the proportional cover of the seawater predicted from the soft classification and that derived from the reference data

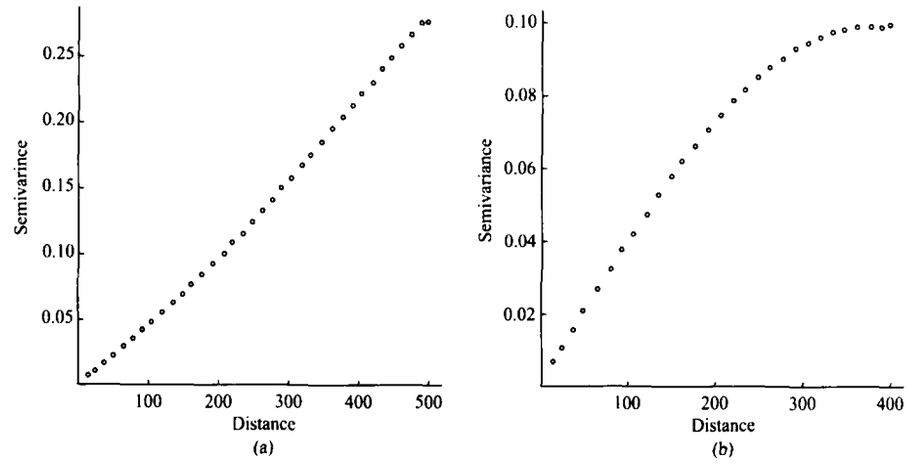


Fig. 3 (a) Experimental indicator variogram based on original data; (b) Detrended experimental indicator variogram

ously systematic trend, therefore the assumption (2) were not satisfied. By decompositing the variable data into trend and residual portion and fitting the trend portion using polynomials, the variogram can be computed properly from the residual portion (Gringarten & Deutsch, 2001). The experiment by Chapell *et al.* (2001) had showed that better result of removing the trend on the remote sensing image could be obtained using second-order polynomials. Therefore, second-order polynomial regression was used to fit the systematic trend existed in the variable data, as the following eqation:

$$Z(x) = S^{\mathrm{T}}(x)\beta + \varepsilon(x) \tag{7}$$

where $S(x)$ was a vector consisting of $(1, x_1, x_2, x_1^2, x_2^2, x_1x_2)$, with $x_1$, $x_2$ being the coordinates of the pixels. $\beta$ was the vector of coefficients, and $\varepsilon(x)$ was a zero-mean random variable representing residuals after removing trend. The experimental variogram was calculated based on $\varepsilon(x)$. Fig. 3(b) was the experimental variogram that had removed the trend, from which it can be seen that the variogram curve reached the sill at 0.10.

### 3.3 Spatial structure models

The variogram for fine-resolution seawater class indicators, the fine-to-coarse variograms between seawater class indicators and corresponding coarse fractions, and the variogram between coarse seawater class fractions were considered as the measurement values of the spatial structure of seawater class. Because variogram values are not statistically reliable at large distances, the maximum calculation distance usually is no longer than half of image extent (Chilès & Delfiner, 1999). Therefore, the maximum distance was set as 400m in this study. A discontinuity of the variogram at the origin called nugget effect can be related to either uncorrected noise (measurement error) or to spatial structures at a length scale smaller than pixel size. The experimental variogram illustrated by Fig. 3(b) was linear at the origin, without any nugget effect; therefore the assumption (3) and (4) were satisfied. The experimental variograms and their variogram model fitting were accomplished in R environment using GSTAT software. The experimental variograms were fitted using Spherical model, as the following equation:

$$\gamma(h) = \begin{cases} c_0 + c_1\left\{\dfrac{3h}{2a} - \dfrac{1}{2}\left(\dfrac{h}{a}\right)^3\right\}, 0 < h < a \\ c_0 + c_1, h \geqslant a \end{cases} \tag{8}$$

where the model parameters were obtained from the experimental variogram curves and these values were considered as the initial estimates of these variogram models. They were nugget coefficient $c_0$=0.002, sill $c_1$=0.097, and range $a$=368m. The fit.lmc method (i.e. "linear model of co-regionalization") was used to adjust the partial sills (Psills) of each model, in order to make sure the subsequent ICK system with positive definite matrixes (as shown in Fig. 4).

### 3.4 Indicator coKriging

Based on 14.25m×14.25m fine resolution pixels as fine-scale grids, the coarse fraction data and fine & coarse resolution indicator variogram models, the probabilities for seawater class occurrence at any fine resolution pixel $v_m$ that fallen within the coarse pixel $V_n$ were computed via ICK. The data used for ICK at pixel $v_m$ consisted of the 4×4 coarse template centered at $V_n$. The resulting set of the seawater probability map generated using Eq. (3) is shown in Fig. 5(a). The resulting ICK-based probabilities can be corrected to ensure that they lie in the [0, 1] interval; however, the magnitude of such correction is very small (Goovaerts, 1997), therefore this correction was ignored in this study. The ICK-derived seawater probabilities were averaged within each coarse pixel, and compared to the corresponding coarse fractions. As shown in Fig. 5(b), the ICK predicted values of the seawater class fraction of the mixed pixels containing coastline information and the observed values of the seawater class fraction derived from the reference data were highly correlated ($R^2$=0.9339), indicating that ICK-derived results can properly maintain the actual information of the seawater class fraction. Solving ICK equation system also determined the CCDF required for the subsequent conditional random simulation.

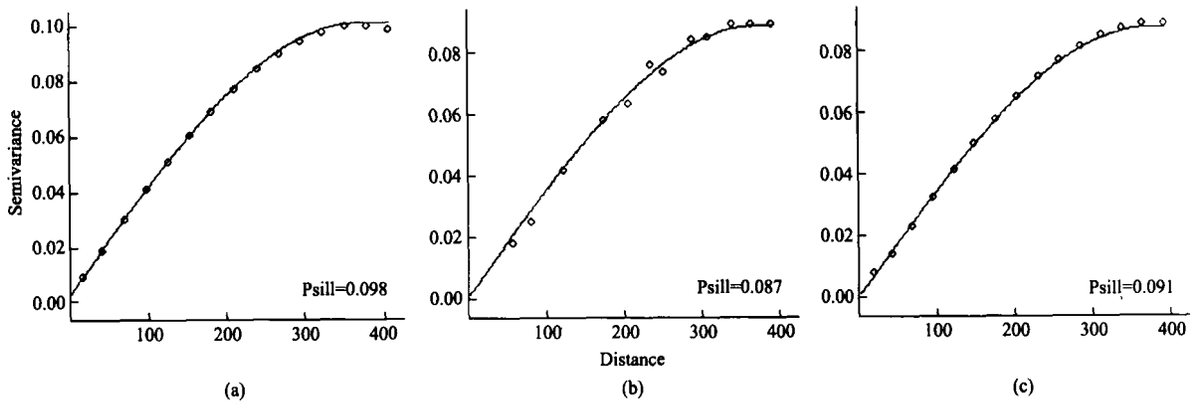


Fig. 4 (a) Fine-resolution indicator variogram; (b) Coarse-resolution fraction variogram; (c) Fine-to-coarse resolution cross-variogram and the fitted linear model of coregionalisation for these variograms

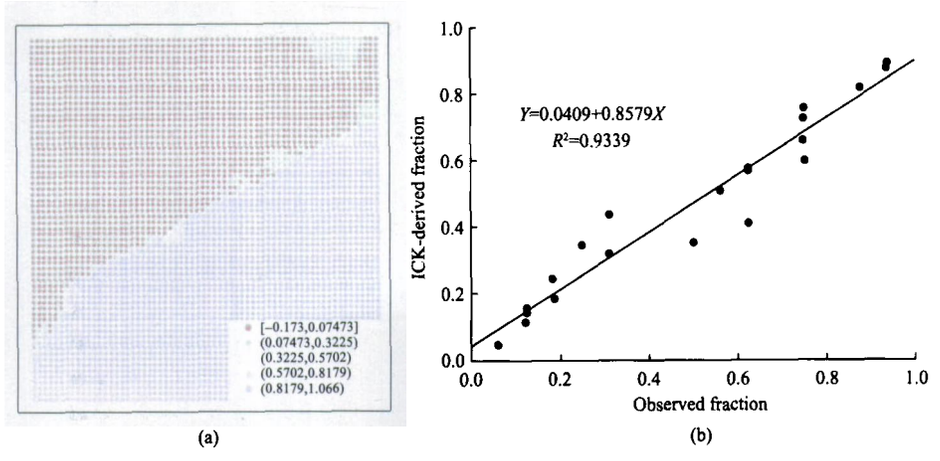


Fig. 5 (a) Conditional probabilities of fine-resolution seawater occurrence computed via simple indicator coKriging (ICK); (b) Relationship between coarse seawater fractions by the ICK-derived probabilities & observed coarse seawater fraction.

### 3.5 Sequential Indicator co-Simulation

Based on 14.25m×14.25m fine resolution pixels as fine scale grids, the coarse fraction data and the CCDF derived from ICK, multiple super-resolution realizations of the seawater class fraction were yielded via SIcS. In order to accommodate the simulated outputs with equal quality as many as possible, 1000 SIcS realizations were generated in this study. The contour map was produced based on the average of their simulated probabilities, and the contour line whose average of its simulated probabilities equal to 0.5 (represented the 50% membership to land and 50% membership to seawater) was considered as the coastline mapping result. With measure methods provided by ESRI ArcObjects, measurement points taken at 1m interval were created from the coastline extracted by human interpretation, and the shortest distances from the measurement points to the coastline derived from supervised classification and from conditional simulation was calculated, to estimate the coastline mapping accuracy. The calculation results showed that the average of the shortest distances to the coastline derived from supervised classification was 213m, while that to the coastline derived from conditional simulation was 3m. Taken human interpretation result using fine resolution imagery as the benchmark in Fig. 6(a), the coastline analysis showed that compared to the coastline derived from supervised classification using original data, the coastline derived from conditional simulation using SIcS imagery can illustrate the spatial distribution feature of the coastline at fine scale more accurately and actually. The comparison result between the variogram of the average of simulated probabilities of SIcS imagery and the variogram model of the coarse seawater class fraction of original data was shown in Fig. 6(b), indicating super-resolution imagery can maintain the spatial structure feature of original data rather well.

### 3.6 Silty coastline mapping results

For the coastline at the Yellow River Estuary (B in Fig. 1), the super-resolution mapping results showed in Fig.7 were obtained using the same methodology adopted in the study at the Yellow River Harbor. The accuracy analysis of coastline mapping showed that the average of the shortest distances to the coastline derived from supervised classification was 11.7m, while that to the coastline derived from conditional simulation was 9.58m. Taken human interpretation result using fine resolution imagery as the benchmark in Fig. 7(a), The coastline analysis showed that compared to the coastline derived from supervised classification using original data, the coastline derived from conditional simulation using SIcS imagery can illustrate the spatial distribution feature of the coastline at fine scale

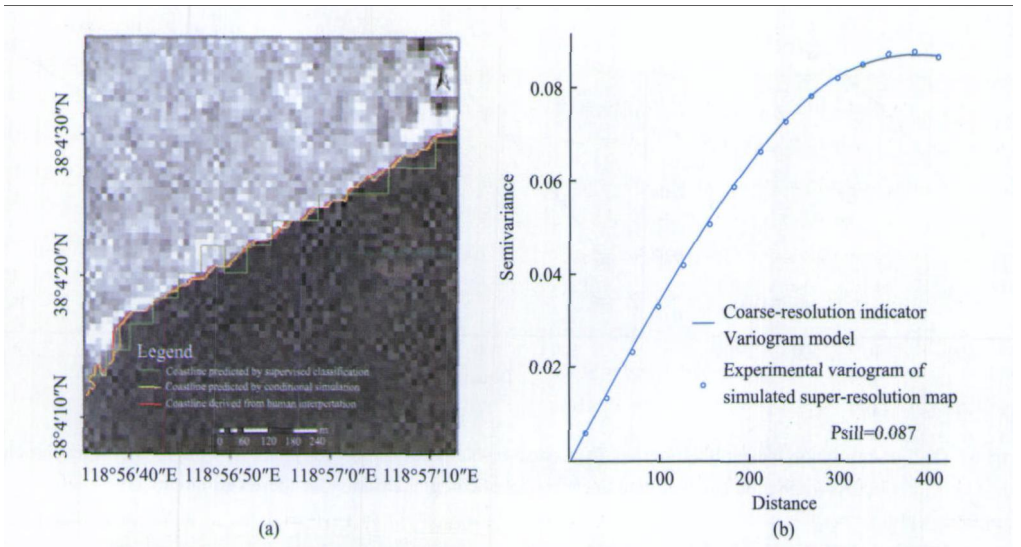


Fig. 6 (a) Coastline predicted from the hard classification applied to the original image VS coastline predicted from the geostatistical approach applied to the SIcS image of A in Fig. 1; (b) Indicator variogram reproduction for super-resolution realization generated conditional to coarse-resolution spatial structure.

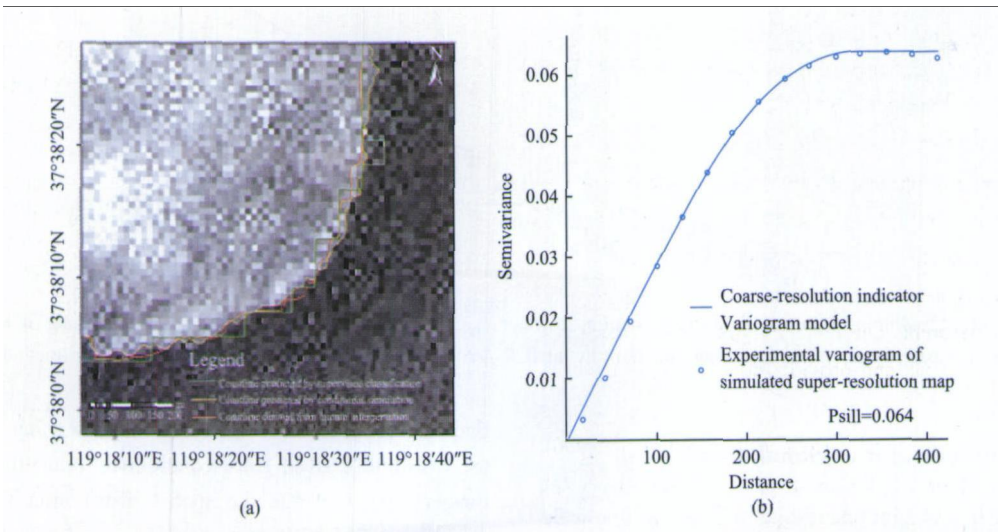


Fig.7 (a) Coastline predicted from the hard classification applied to the original image VS coastline predicted from the geostatistical approach applied to the SIcS image of B in Fig.1; (b) Indicator variogram reproduction for super-resolution realization generated conditional to coarse-resolution spatial structure.

more actually. In Fig. 7(b), the Psill value of the variogram of the average of simulated probabilities of SIcS imagery was 0.064, close to the Psill value (0.068) of the variogram of the coarse seawater class fraction of original data. In general, the super-resolution mapping accuracy of the silty coastline was lower than that of the artificial coast.

## 4 CONCLUSION AND DISCUSSION

The total length of coastline in China is more than 32,000km, extending northward to the Yalujiang estuary, southward to the Beilun River estuary (Cui, 1998). Therefore, it is necessary for coastal investigation and mapping at regional scale to use remotely sensed data with a variety of spatial resolution, even though remotely sensed data with higher spatial accuracy are increasingly rich. The remotely sensed data used for coastal research mainly include synthetic aperture radar (SAR), near infrared, shortwave infrared, and thermal infrared images. Wherein, SAR sensor seems unlikely to be widely applied to coastal research at present for few archived data. Among the passive optical sensors, higher spatial resolution images (such as IKONOS and Quickbird), and recently developed LIDAR and InSAR techniques have enough abilities to get higher accuracy in coastline detection, but obtaining such data means higher costs. By contrast, the moderate spatial resolution images are cost-effective and informative, wherein the Landsat platforms have been providing repetitive, synoptic, and global coverage of multispectral moderate resolution images with relatively high frequency for over 30 years, especially suitable for coastal information extraction and analysis at regional scale. In this paper, the philosophy of super-resolution mapping was introduced into coastline extraction and mapping based on

remotely sensed data with moderate spatial resolution. Geostatistical techniques such as Kriging and conditional simulation were used to integrate spectral and spatial information of remotely sensed data, and the spatial distribution of land & ocean environment were mapped at fine scale. The experiment results showed that the prior information contained within the fine resolution variogram was integrated into the simulated images of land & ocean classes generated from cokriging and conditional co-simulation techniques. Super- resolution maps illustrated the spatial distribution of coastline at fine scale rather well, meanwhile maintained the ocean & land class fractions and their spatial structures contained within the original data.

In general, super-resolution mapping technique based on prior model of spatial structure, explores probability distribution of unknown classes at target scale using multiple simulated realizations derived from the data or information at original scale. The significance of this technique is not for obtaining more accurate super-resolution images of spatial distribution of coastline or any other earth cover types, but for exploring possible realizations of unknown classes at target scale from information with variety of scales or accuracies, and these realizations are matched with available information at present. Here, the concept of mapping accuracy can be understood as simulated realizations actually maintain this available information and their spatial structure as much as possible. Super-resolution maps can be served as inputs to detailed spatial analysis environment, coupled environmental models, or decision support systems, and provide the uncertainty analysis framework due to lacking proper resolution information used in the above operations or models (Boucher & Kyriakidis, 2006). By the form of super-resolution mapping of coastline, the potential of geostatistical techniques in integrating multi-source and multi-scale spatial information has been demonstrated. The research objectives in this study are rather simple artificial and silty coast. In terms of more complicated coastal environment such as Yangzi River estuary or Hangzhou Bay, it is important to build prior model of spatial structure with higher quality, and ground investigation or expert knowledge can be integrated into inferring process of prior model of spatial structure. In addition, recent-developed multi-point geostatistics theory adopts training image instead of variogram, expected to overcome the insufficiency of two-point geostatistics on characterizing complex spatial patterns and reproducing crisp geometrics (Boucher *et al.*, 2008).

## REFERENCES


Atkinson P M and Curran P J. 1995. Defining an optimal size of support for remote-sensing investigations. *IEEE Transactions on Geoscience and Remote Sensing*, **33**(3): 768—776

Atkinson P M, Cutler M E J and Lewis H. 1997. Mapping sub-pixel proportional land cover with AVHRR imagery. *International Journal of Remote Sensing*, **18**(4): 917—935

Atkinson P M. 1997. Mapping sub-pixel boundaries from remotely sensed images. Kemp Z. Innovations in GIS 4. London: Taylor and Francis

Atkinson P M. 2004. Super-resolution land cover classification using two-point histogram. X Sanchez-Villa and Carrera J G H J. GeoENV IV Geostatistics for Environmental Applications, New York: Springer-Verlag

Boak E H and Turner I L. 2005. Shoreline definition and detection: a review. *Journal of Coastal Research*, **21**(4): 688—703

Boucher A and Kyriakidis P C. 2006. Super-resolution land cover mapping with indicator geostatistics. *Remote Sensing of Environment*, **104**(3): 264—282

Boucher A, Kyriakidis P C and Cronkite-Ratcliff C. 2008. Geostatistical solutions for super-resolution land cover mapping, *IEEE Transactions on geosciences and remote sensing*, **46**(1): 272—283

Carle S F and Fogg G E. 1996. Transition probability-based indicator geostatistics. *Mathematical Geology*, **28**(4): 453—476

Carr J R, Bailey R E and Deng E D. 1985. Use of indicator variograms for an enhanced spatial analysis. *Mathmatical Geology*, **17**(8): 797—811

Chappell A, Seqquist J W and Eklundh L. 2001. Improving the estimation of noise from NOAA AVHRR NDVI for Africa using geostatistics, *International Journal of Remote Sensing*, **22**: 1067—1080

Chen S L, Zhang G A and Gu G C. 2004. Mechanism of heavy coastal erosion on Yellow River Delta and its countermeasures. *Journal of Hydraulic Engineering*, **7**: 1—7, 16

Chilès J P and Delfiner P. 1999. Geostatistics: modeling spatial uncertainy. New-York: Wiley Inter-Science

Cui N F. 1998. The Gazetteer of the People's Republic of China: vol 1. Beijing: The Commercial Press

Foody G M, Muslim A M and Atkinson P M. 2005. Super-resolution mapping of the waterline from remotely sensed data. *International Journal of Remote Sensing*, **24**: 5381—5392

Foody G M. 1996. Approaches for the production and evaluation of fuzzy land cover classifications from remotely sensed data. *International Journal of Remote Sensing*, **17**: 1317—1340

Frazier P S and Page K J. 2000. Water body detection and delineation with Landsat TM data. *Photogrammetric Engineering and Remote Sensing*, **66**(12): 1461—1467

Garrigues S, Allard D, Baret F and Weiss M. 2006. Quantifying spatial heterogeneity at the landscape scale using variogram models. *Remote Sensing of Environment*, **103**: 81—96

Goovaerts P. 1997. Geostatistics for Natural Resources Evaluation. New York: Oxford University Press

Gringarten E and Deutsch CV. 2001. Variogram interpretation and modeling. *Mathematical Geology*, **33**(4): 507—534

Journel A G and Alabert F. 1989. Non-Gaussian data expansion in the earth sciences. *Terra Nova*, **1**(2): 123—134

Journel A G and Huijbregts C J. 1978. Mining Geostatistics. San Diego: Academic Press

Journel A G. 1983. Nonparametric estimation of spatial distributions. *Mathematical Geology*, **15**(3): 445—468

Malthus T J and Mumby P J. 2003. Remote sensing of the coastal zone: an overview and priorities for future research. *International Journal of Remote Sensing*, **24**: 2805—2815

Manavalan P, Sathyanath P and Rajegowda G L. 1993. Digital image analysis techniques to estimate waterspread for capacity evaluations of reservoirs. *Photogrammetric Engineering and Remote Sensing*, **59**(9): 1389—1395

Muslim A M, Foody G M and Atkinson P M. 2007. Shoreline mapping from coarse-spatial resolution remote sensing imagery of Seberang Takir, Malaysia. *Journal of Coastal Research*, **23**(6): 1399—1408

Ryu J H, Won J S and Min K D. 2002. Waterline extraction from Landsat TM data in a tidal flat: a case study in Gomso Bay, Korea, *Remote Sensing of Environment*, **83**: 442—456

Shen F, Gao A, Wu J P, Zhou Y X and Zhang J. 2008. A Remotely sensed approach on waterline extraction of silty tidal flat for DEM construction, a case study in Jiuduansha Shoal of Yangtze River, Acta Geodaetica et Cartographica Sinica, **37**(1): 102—107

Southworth J. 2004. An assessment of Landsat TM Band 6 thermal data for analyzing land cover in tropical dry forests. *International Journal of Remote Sensing*, **25**(4): 689—706

Tatem A J, Lewis H G, Atkinson P M and Nixon M S. 2003. Increasing the spatial resolution of agricultural land cover maps using a Hop field neural network. *International Journal of Geographical Information Science*, **17**(7): 647—672

Verhoeye R and De Wulf J. 2002. Land cover mapping at sub-pixel scales using linear optimization techniques. *Remote Sensing of Environment*, **79**(1): 96—104

Zhang Y and Chen S L. 2009. Remote sensing analysis of spatial-temporal pattern on coastline change: a case study in the abandoned Yellow River Delta Coast. *Advances in Marine Science*, **27**(2): 166—175

# 结合遥感数据与地统计学方法的海岸线超分辨率制图

张　旸, 陈沈良

华东师范大学 河口海岸学国家重点实验室, 上海　200062

**摘　要:** 使用黄河三角洲海岸 Landsat 卫星遥感数据, 基于研究区域低分辨率 6 波段的海陆类型软分类结果及其变差函数, 以高分辨率 8 波段的指示变差函数为精细尺度先验信息模型, 采用数据探索性分析、协同指示克里格和序贯指示协同模拟技术, 生成海陆类型发生概率模拟图像, 通过等值线法提取海岸线空间分布特征。实验表明, 基于地统计学方法的超分辨率制图技术在低分辨率遥感数据中融合高分辨率空间结构先验模型, 可以较好表达精细尺度上的海岸线空间分布特征, 同时保持原始数据的海陆类型组分信息及其空间结构特征。地统计学方法集成多尺度乃至多源空间信息的潜力通过海岸线超分辨率制图形式得到展示。

**关键词:** 遥感数据, 地统计学, 海岸线, 超分辨率制图, 黄河三角洲

**中图分类号:** TP79/P237　　**文献标识码:** A

**引用格式:** 张　旸, 陈沈良. 2010. 结合遥感数据与地统计学方法的海岸线超分辨率制图. 遥感学报, 14(1): 148—164
Zhang Y, Chen S L. 2010. Super-resolution mapping of coastline with remotely sensed data and geostatistics. *Journal of Remote Sensing*. 14(1): 148—164

## 1　引　言

海岸线是陆地和海洋的交界线, 其位置随时间发生连续变化, 本质上是动态的(Boak & Turner, 2005)。获取海岸线位置及其变化信息是海岸环境监测与管理的基础内容。由于海岸的特殊自然环境及动态特性, 传统的野外观测方法费时费力且代价昂贵, 卫星遥感技术作为一种快速并且廉价的数据收集方法广泛应用于海岸信息获取与动态监测工作中(张旸等, 2009)。据国家标准《中国海图图式》(GB12319-1998)和国家标准《1∶5000, 1∶10000 地形图图式》(GB/T5791-93), 海岸线的标准定义是指平均大潮高潮时海陆分界的痕迹线, 此线并非实际存在, 在遥感图像上通常使用水边线表示海陆分界线。遥感数据中的近红外(如 Landsat TM 4)和短波红外(如 Landsat TM 5)波段对于提取砂质海岸或清澈水体边界信息的效果较好(Manavalan 等, 1993; Frazier & Page, 2000)。在影响因素复杂的淤泥质潮滩, 热红外波段对水边线位置最为敏感(Ryu 等, 2002; 沈芳等, 2008), 但是空间分辨率不高(在 Landsat TM/ETM+和 EOS-Terra ASTER 中分别为 120m/60m 和 90m)。此外, 中等分辨率传感器瞬时视场所观测的地表一般呈空间异质性, 连同水深变化和海水混浊等因素形成混合像元, 影响着海岸线信息提取与制图的精度(Malthus & Mumby, 2003)。

目前解决混合像元问题的主要方法是混合像元分解, 即通过各种模糊或软分类器估算混合像元内部各种类型组分的比例(Foody, 1996)。该方法可以提供比基于单个像元的硬分类方法更加精确和适宜的类型组分信息, 但是无法确定混合像元内部各类型组分的空间分布位置(Atkinson, 1997)。针对该问题发展了许多在子像元尺度上定位类型组分地理分布的方法, 并且在土地利用/土地覆盖制图中得到成功应用(Tatem 等, 2003; Boucher & Kyriakidis, 2006)。这些方法旨在超越原有数据的空间分辨率限制, 在

**收稿日期:** 2008-10-20; **修订日期:** 2009-05-31

**基金项目:** 海洋公益性行业科研专项经费项目(编号: 200805063)和河口海岸学国家重点实验室科研业务课题(编号: 2008 KYYW06)。

**第一作者简介:** 张旸(1975— ), 男, 博士后, 2007 年毕业于中国科学院地理科学与资源研究所地图学与地理信息系统专业, 目前主要从事海岸带遥感与地理信息系统应用研究。E-mail: zhangyang2907@163.com。

一个更加精细的尺度上反映地表类型信息，被称为超分辨率制图方法。超分辨率技术在海岸线制图方面的潜力通过模拟场景试验得到了展示(Foody 等, 2005; Muslim 等, 2007)。超分辨率制图可归于反问题理论范畴，即根据低分辨率类型数据再现这些类型在精细尺度上的空间分布特征(Boucher 等, 2008)。由于该反问题具有非充分决定性的特点，因此需要使用先验信息(比如精细尺度上的空间结构先验模型)指导类型单元空间格局的再现过程。该先验模型可基于最大空间连续性假设(Atkinson 等, 1997; Verhoeye & De Wulf, 2002)，或是地统计学分析中的变差函数(Atkinson, 2004; Boucher & Kyriakidis, 2006)。本文基于地统计学原理，以真实场景遥感图像的像元值为区域化变量，在目标图像的海陆光谱分类中融合原始数据与精细尺度的空间结构特征模型，以此为基础进行海岸线超分辨率制图研究。

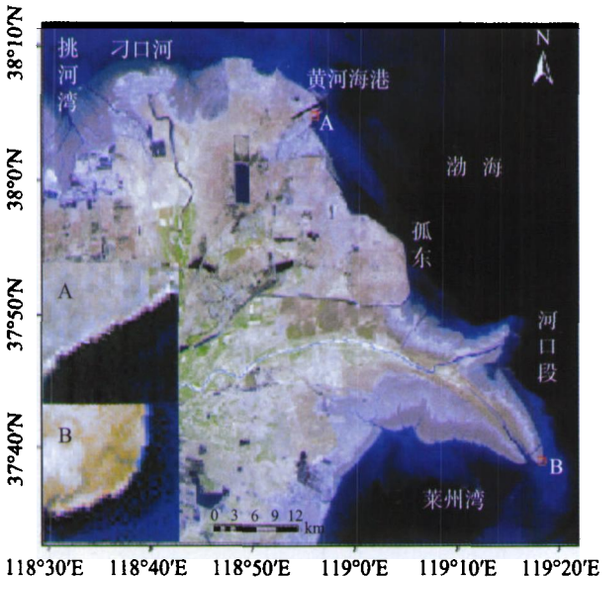


图 1 2000 年 Landsat-7 ETM+图像的研究区位图

## 2 材料与方法

### 2.1 研究区与数据描述

黄河三角洲是 1855 年黄河于铜瓦厢决口注入渤海后发育而成，它是中国乃至世界各大河三角洲中海陆变迁最活跃的地区之一。由于河流与海洋 2 种动力的强烈作用，黄河三角洲的海岸线不断发生着淤蚀交替的演变过程。根据近年来的海岸侵淤状况可分为弱侵蚀、强侵蚀和强堆积海岸。弱蚀型海岸主要分布在挑河湾以西；强蚀型海岸主要分布在挑河湾以东的刁口河、神仙沟和孤东岸段；强堆积型海岸主要分布在黄河现行河口及其两侧(陈沈良等, 2004)。本文的研究区域位于黄河海港段的人工海岸(图 1 中 A)和黄河河口段的淤泥质海岸(图 1 中 B)，海港段海岸由于修建了防护堤，近年来变化不大；而河口段海岸在河流与海洋动力作用下变化迅速。

用于地统计学分析的遥感数据需要满足以下假设：(1) 各波段之间的配准误差足够小；(2) 图像范围能容纳待测变量的空间特征；(3) 辐射测量误差相对地表变化较小；(4) 小于传感器采样间距的空间变异效应可以忽略不计(Garrigues 等, 2006)。本文选取 2000-05-02 的 Landsat-7 ETM+热红外 6 波段(空间分辨率 60m，像元尺寸 57m)作为海岸线制图的低分辨率遥感数据源。热红外波段直接与地表覆盖相关联，与反射波段分属不同的测量系统，在相同像元范围内与其他 TM 波段联合用于监测或记录信息分析，及时且节约成本(SouthWorth, 2004)。采用全色 8 波段(空间分辨率 15m，像元尺寸 14.25m)作为精细尺度先验信息数据源，旨在保证统一的使用数据成像环境，避免制图数据和参考数据之间的配准误差和时相误差，以满足假设(1)。表 1 为研究使用的 Landsat 数据概况描述。

### 2.2 研究方法

研究方法以 Boucher & Kyriakidis (2006)提出的指示地统计学技术框架为基础，结合海陆遥感光谱对比特征设计而成，简述如下：

#### 2.2.1 类型指标与组分

设 $c(v)$表示一个高分辨率像元 $v=v(\boldsymbol{u})$的未知类型(海水或陆地)，面积为$|v|$，$\boldsymbol{u}$ 是像元中心的坐标向量。所有像元的未知类型组成$(M\times 1)$向量 $\boldsymbol{c}=[c(v_m), m=1,\cdots,M]^{\mathrm{T}}$，$M$ 为高分辨率像元数目。通过二元指示函数 $i(v)$表示像元 $v$ 是否属于海水类型，是则 $i(v)=1$，否则为 0。所有海水类型指标组成$(M\times 1)$向量 $\boldsymbol{i}=[i(v_m), m=1,\cdots,M]^{\mathrm{T}}$。设 $a(V)$表示一个低分辨率像元 $V=V(\boldsymbol{s})$中的海水类型组分，该像元面积为$|V|$，$\boldsymbol{s}$ 是像元中心坐标向量。海水类型组分值组成$(N\times 1)$向量 $\boldsymbol{a}=[a(V_n), n=1,\cdots,N]^{\mathrm{T}}$，$N$ 为低分辨率像元数目。$F=|V|/|v|=M/N>>1$ 表示低和高分辨率图像的分辨率比率。由于图像经过配准，一个低分辨率像元 $V$ 包含 $F$ 个高分辨率像元$\{v_m, m=1,\cdots,F\}$。超分辨率制图目标即为从类型组分向量 $\boldsymbol{a}$ 中求解未知类型向量 $\boldsymbol{c}$ (Boucher & Kyriakidis, 2006)。

#### 2.2.2 指示变差函数

精细尺度海水类型的空间分布特征可由其平稳比例和高分辨率图像空间结构度量值来表示，设 $\delta$

为海水类型的平稳比例。在低分辨率像元 $V_n$ 中，海水类型组分值 $a(V_n)$设为在 $V_n$ 内的 $F$ 个高分辨率像元的海水类型指示值的均值，即

$$a(V_n)=\frac{1}{F}\sum_{m=1}^{F} i(v_m), v_m \in V_n \tag{1}$$

低分辨率海水类型组分的均值 $\bar{a}$ 等于海水类型平稳比例 $\delta$:

$$\bar{a}=\frac{1}{N}\sum_{n=1}^{N} a(V_n)=\frac{1}{N}\sum_{n=1}^{N}[\frac{1}{F}\sum_{m=1}^{F} i(v_m)]$$
$$=\frac{1}{M}\sum_{m=1}^{M} i(v_m)=\delta \tag{2}$$

指示变差函数 $2\gamma^{v}(\boldsymbol{h})$ 表示由矢量 $\boldsymbol{h}$ 分隔的两个高分辨率像元之间的联合概率(Carle & Fogg, 1996)，上标 $v$ 代表 $2\gamma^{v}(\boldsymbol{h})$与 $v$ 个高分辨率像元相关。$2\gamma^{v}(\boldsymbol{h}_{mm'})=2\gamma^{v}(\boldsymbol{u}_m-\boldsymbol{u}_{m'})$表示两个未知类型高分辨率像元 $v_m$ 和 $v_{m'}$ 的海水类型指示变差函数，其中心点 $\boldsymbol{u}_m$ 和 $\boldsymbol{u}_{m'}$由 $\boldsymbol{h}_{mm'}=\boldsymbol{u}_m-\boldsymbol{u}_{m'}$分隔。设海水类型的高分辨率变差函数模型为 $2\gamma^{v}(\boldsymbol{h};\boldsymbol{\theta})$，$\boldsymbol{\theta}$ 为模型参数向量。高分辨率像元 $v_m$ 的海水类型指示函数 $i(v_m)$和低分辨率像元 $V_n$ 的海水类型组分 $a(V_n)$之间的变差函数为像元中心 $\boldsymbol{u}_m$ 和 $\boldsymbol{s}_n$ 的分隔向量 $\boldsymbol{h}_{mn}$ 的函数，即

$$2\gamma(v_m;V_n)=2\gamma(v(\boldsymbol{u}_m);$$
$$V(\boldsymbol{s}_n))=2\gamma^{vV}(\boldsymbol{u}_m-\boldsymbol{s}_n)=2\gamma^{vV}(\boldsymbol{h}_{mn})$$

式中，上标 $vV$ 表示 $2\gamma^{vV}(\boldsymbol{h}_{mn})$ 是 $v$ 个高分辨率像元和 $V$ 个低分辨率像元之间的交叉分辨率变差函数。两个低分辨率像元 $V_n$ 和 $V_{n'}$的海水类型组分之间的变差函数是像元中心 $\boldsymbol{s}_n$ 和 $\boldsymbol{s}_{n'}$的分隔向量 $\boldsymbol{h}_{nn'}$的函数，即

$$2\gamma(V_n;V_{n'})=2\gamma(V(\boldsymbol{s}_n);$$
$$V(\boldsymbol{s}_{n'}))=2\gamma^{V}(\boldsymbol{s}_n-\boldsymbol{s}_{n'})=2\gamma^{V}(\boldsymbol{h}_{nn'}),$$

式中，上标 $V$ 表示 $2\gamma^{V}(\boldsymbol{h}_{nn'})$ 是 $V$ 个低分辨率像元之间的低分辨率变差函数 (Boucher & Kyriakidis, 2006)。高分辨率像元海水类型的指示变差函数模型，海水类型指标与低分辨率类型组分之间的变差函数，以及低分辨率海水类型组分之间的变差函数被用来估算任意高分辨率像元上海水类型发生的概率(Journel & Huijbregts, 1978; Atkinson & Curran, 1995)。

**表 1 研究使用的 Landsat 数据像元值的描述性统计**

| 数据 | 像元数 | 最小值 | 最大值 | 均值 | 中值 | 方差 | 峰度 | 偏度 |
|---|---|---|---|---|---|---|---|---|
| Band6 (A) | 16×16 | 125 | 173 | 146.70 | 143 | 354.58 | 1.15 | 0.09 |
| Band8 (A) | 64×64 | 21 | 103 | 59.78 | 53 | 256.32 | 1.46 | 0.19 |
| Band6 (B) | 16×16 | 121 | 165 | 142.65 | 143 | 301.37 | 1.15 | 0.03 |
| Band8 (B) | 64×64 | 36 | 83 | 56.92 | 57 | 82.61 | 2.02 | 0.17 |

### 2.2.3 指示协同克里格

指示协同克里格(Indicator CoKriging, ICK)方法以低分辨率组分数据 $\boldsymbol{a}(V)$为基础，可以生成任意高分辨率像元 $v$ 的海水类型发生概率 $p(v)$= Prob{$I(v)$= 1|$\boldsymbol{a}$}的近似值 $\hat{p}(v)$ ( Journel, 1983; Goovaerts, 1997)。由海水类型比例已知，通过简单 ICK 估算高分辨率像元 $v_m$:

$$\hat{p}(v_m)=\boldsymbol{\eta}(v_m)^{\mathrm{T}}\boldsymbol{a}+\delta[1-\boldsymbol{\eta}(v_m)^{\mathrm{T}}\boldsymbol{1}_N] \tag{3}$$

其中 $\boldsymbol{\eta}(v_m)=[\eta_n(v_m), n=1,...,N]^{\mathrm{T}}$ 表示由 $N$ 个海水类型组分的权重组成的$(N\times 1)$向量，$\boldsymbol{1}_N$表示 1 的 $(N\times 1)$向量，已知海水类型比例 $\delta$ 作为$\boldsymbol{\eta}(v_m)$ $\boldsymbol{1}_N$补集的权重。求解以下方程可获得海水类型的 ICK 权重$\boldsymbol{\eta}(v_m)$:

$$\Gamma^{VV}\boldsymbol{\eta}(v_m)=\gamma^{vV}(v_m) \tag{4}$$

其中，$\Gamma^{VV}=[2\gamma^{V}(\boldsymbol{h}_{nn'}), n=1,...,N, n'=1,...,N]$ 是所有低分辨率像元对之间的组分变差函数值的$(N\times N)$矩阵，$\gamma^{vV}(v_m)=[2\gamma^{vV}(\boldsymbol{h}_{mn}), n=1,...,N]^{\mathrm{T}}$ 表示未知类型高分辨率像元 $v_m$ 和 $N$ 个低分辨率像元之间变差函数值的$(N\times 1)$向量。

### 2.2.4 序贯指示协同模拟

序贯指示协同模拟 (Sequential Indicator co-Simulation, SIcS)方法根据已知类型样本数据和指示变差函数模型生成模拟的海陆类型合成图(Journel & Alabert, 1989; Goovaerts, 1997)。SIcS 将 M 个指示随机变量{$I(v_m)$, $m$=1,...,$M$}的多变量概率分布函数 $\int(i|\boldsymbol{a})$分解为 $M$ 个单变量条件概率序列:

$$\int(i|\boldsymbol{a})=\mathrm{Prob}\{I(v_1)=i(v_1),...,I(v_M)$$
$$=i(v_M)|\boldsymbol{a}\}=\prod_{m=1}^{M}\mathrm{Prob}\{I(v_m)=1|i^{m-1},\boldsymbol{a}\} \tag{5}$$

其中，$\mathrm{Prob}\{I(v_m)=1|i^{m-1},\boldsymbol{a}\}$是由 ICK 生成的指示随机变量 $I(v_m)$的条件累积分布函数(ccdf)，先前已模拟的 $m$−1 个海水类型指标存储在$((m-1)\times 1)$向量 $i^{m-1}=[i(v_{m'}), m'=1,...,m-1]^{\mathrm{T}}$ 中，原始数据向量 $\boldsymbol{a}$ 包括 $N$ 个低分辨率海水类型组分。模拟的随机路径由 $M$ 个高分辨率像元序列组成，它确定了式(5)的分解顺序。对于路径上的任意高分辨率像元 $v_m$，由相对应的条件概率产生模拟类型属性 $c(v_m)$。相关联的模

拟类型指标 $i(v_m)$指导所有随后产生的单变量条件概率及其模拟类型属性。对所有 $M$ 个高分辨率像元重复以上步骤得到类型属性的模拟实现，表示为 $c=[c(v_m),\ m=1,\ldots,M]^T$。新的类型属性模拟实现可以通过不同随机路径重复以上步骤产生(Goovaerts, 1997)。

## 3 研究结果

### 3.1 混合像元分解

对于黄河海港段海岸(图 1 中 A)，根据低分辨率图像采用基于分类的方法进行海岸线制图，划分陆地和海水 2 种类型。采用传统的监督分类方法预测低分辨率图像上的海岸线，以此作为基准数据。使用 IDRISI 软件 FUZZY 模块提供的模糊集成函数执行图像软分类，其结果为每个像元海水类型组分的预测值(图 2(a))。该组分预测值代表了被海水覆盖的像元面积比率，其余部分归于陆地类型。由于不含岸线信息的纯净海水像元软分类结果通常具有高但非 1.0 的组分值，因此将这部分像元组分预测值设为 1.0，以消除其潜在影响。不含岸线信息的纯净陆地像元相应设为 0。处理后的软分类结果作为低分辨率图像的海水类型组分数据。图 2(b)比较了包含岸线信息混合像元的海水类型组分预测值与根据参考数据计算所得的实测值，相关系数为 $R^2$=0.9126，表明该软分类结果可为超分辨率制图提供良好基础。

### 3.2 数据探索性分析

地统计学分析的首要步骤是建立正确的变量数据并使其属性满足平稳假设(Gringarten & Deutsch, 2001)。当变量数据呈偏态分布或存在异常值时，实验变差函数会受其影响表现异常。本文采用的指示地统计学方法可以消除变差函数对异常值的敏感程度，并具有分布自由特性(Carr 等, 1985)。对每一个像元观测值 $Z(x_i)$ $i$=1,2,…,$n$，定义其对应的指示函数值如下式:

$$I(x)=\begin{cases}1, x \leqslant v_c \\ 0, x > v_c\end{cases} \tag{6}$$

式中，阈值 $V_C$ 根据高分辨率图像海水像元值的变化范围确定，图 3(a)为原始数据经指示变换后的实验变差函数。

由图 1 可见，遥感图像中由海岸线组成的海陆空间结构特征明显超越研究区域范围。图 3(a)中的指示变差函数曲线在最大理论基台值 0.25 之上仍然保持增长，表明数据存在明显系统趋势，不满足平稳假设(2)。可将变量数据分解为趋势和剩余 2 部分，通过多项式拟合趋势部分，使用剩余部分计算变差函数(Gringarten & Deutsch, 2001)。实验证明应用二次多项式去除遥感图像趋势的效果较好(Chapell 等, 2001)，因此本文采用二次多项式回归(式(7))拟合变量中的系统趋势:

$$\boldsymbol{Z}(x)=\boldsymbol{S}^{\mathrm{T}}(x)\boldsymbol{\beta}+\varepsilon(x) \tag{7}$$

式中，$\boldsymbol{S}(x)$为$(1, x_1, x_2, x_1^2, x_2^2, x_1x_2)$型向量，$x_1$, $x_2$ 为像元坐标值，$\boldsymbol{\beta}$是系数向量，$\varepsilon(x)$是均值为 0 的随机变量，代表去除趋势后的剩余部分。实验变差函数根据 $\varepsilon(x)$ 计算得到。图 3(b)为去除趋势后的实验变差函数，曲线在 0.10 附近达到了基台值。

### 3.3 空间结构特征模型

以低分辨率海水类型组分之间的变差函数、高分辨率图像的海水类型指示变差函数，以及海水类

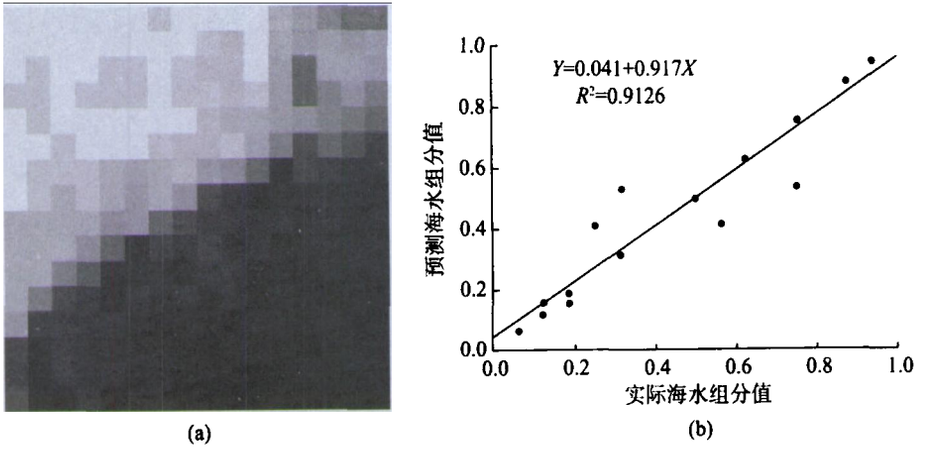


(a) (b)

图 2 (a) 研究区域低分辨率图像的模糊软分类结果。灰度值表示像元属于海水类型的概率，并作为海水所占像元面积比率的估计值；其中白色为纯净陆地区域，黑色为纯净海水区域。(b) 包含岸线信息混合像元的软分类海水组分预测值与根据参考数据计算得到的实测海水组分值之间的关系

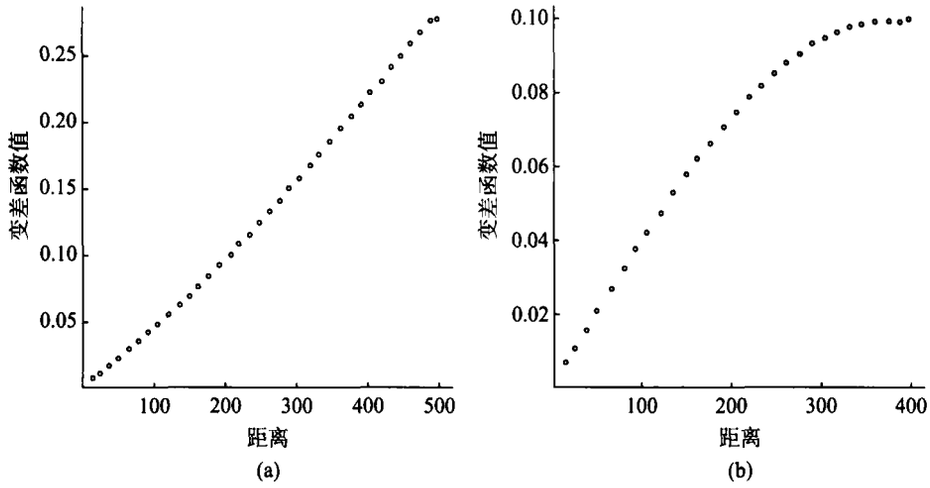


图 3　(a) 基于原始数据的实验指示变差函数; (b) 去除趋势以后的实验指示变差函数

型指标与相应的低分辨率类型组分之间的变差函数作为海水类型空间结构特征的度量值。由于变差函数值在长距离范围不具备统计意义上的可靠性，因此其最大计算距离通常小于 1/2 图像范围(Chilès & Delfiner, 1999)，本文设为 400m。变差函数在坐标原点的不连续性表现为块金效应，主要由无关噪音(测量误差)或空间结构小于像元尺寸引起。图 3(b)所示实验变差函数在原点处呈线性行为，无明显块金效应，因而满足假设(3)与(4)。实验变差函数计算及变差函数模型拟合在 R 语言环境中使用 gstat 程序包完成。实验变差函数采用球状模型拟合，如下式:

$$\gamma(h)=\begin{cases}c_0+c_1\left\{\dfrac{3h}{2a}-\dfrac{1}{2}\left(\dfrac{h}{a}\right)^3\right\}, 0<h<a\\ c_0+c_1, h\geqslant a\end{cases} \tag{8}$$

其中模型参数由实验变差函数曲线特征读取并作为 3 个变差函数模型的初始估计值，分别为块金系数 $c_0$=0.002，拱高(Psill) $c_1$= 0.097，变程 $a$=368m。采用 fit.lmc 方法(即"linear model of co-regionalization")调整每个模型的拱高，以保证随后的协同克里格系统具有正定矩阵(图 4)。

### 3.4　指示协同克里格

ICK 以 14.25m × 14.25m 高分辨率像元为精细尺度网格，使用低分辨率组分数据和高低分辨率指示变差函数模型，求得位于低分辨率像元 $V_n$ 内的任意高分辨率像元 $v_m$ 的海水类型发生概率。在像元 $v_m$ 上用于 ICK 的数据包括以 $V_n$ 为中心的 4 × 4 低分辨率模板。图 5(a)为使用式(3)生成的海水类型发生概率图。ICK 结果可以通过校正保证其位于[0, 1]之间，但是这样的校正意义不大(Goovaerts, 1997)，因此本文不做校正处理。图 5(b)对 ICK 生成的海水类型发生概率在低分辨率尺度上进行均值化，并与相对应的低分辨率组分比较。如图 5 所示，包含岸线信息混合像元的海水类型组分 ICK 预测值与根据参考数据计算所得的海水类型组分实测值之间的相关系数为 $R^2$=0.9339，由此可见 ICK 结果可以较好的保持实际海水类型组分信息。求解 ICK 方程组也确定了随后的条件随机模拟所需的条件累积分布函数(ccdf)。

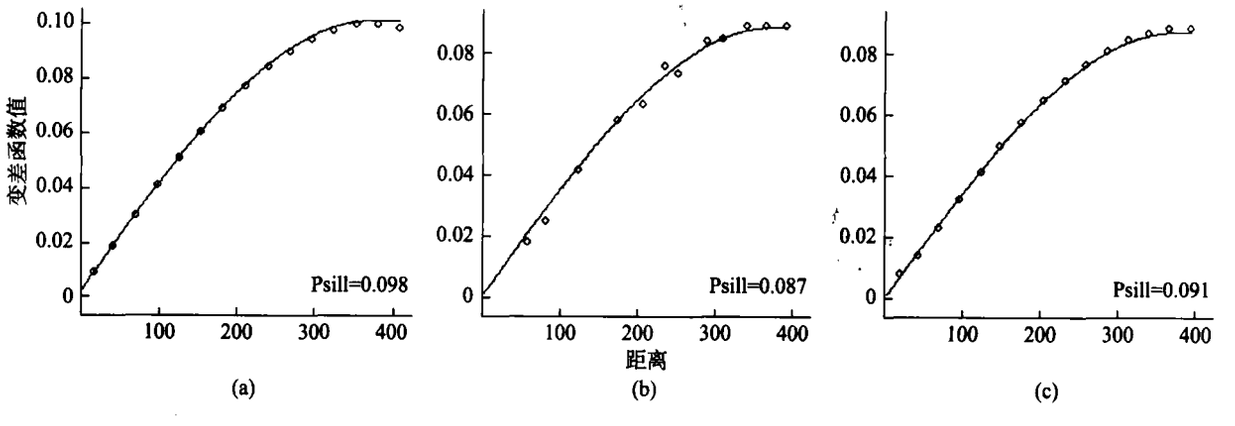


图 4　(a) 高分辨率指示变差函数; (b) 低分辨率类型组分的变差函数; (c) 高分辨率与低分辨率之间的交叉变差函数以及它们的变差函数模型曲线

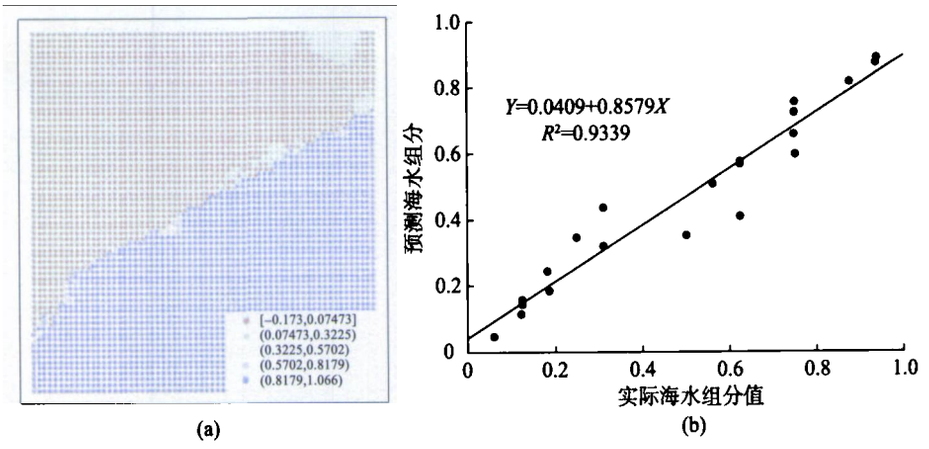


(a) (b)

图 5 (a) 由 ICK 计算得到的精细尺度海水类型发生的条件概率; (b) 包含岸线信息混合像元的海水类型组分 ICK 预测值与根据参考数据计算所得的海水类型组分实测值之间的相关关系

### 3.5 序贯指示协同模拟

SIcS 以 14.25m × 14.25m 高分辨率像元为精细尺度网格，使用低分辨率组分数据和由 ICK 生成的条件累积分布函数，模拟多个海水类型组分的超分辨率实现(realization)图像。为了尽可能多的容纳具有同等质量的模拟输出结果，本文生成 1000 个 SIcS 实现图像。根据其模拟概率值的均值绘制等值线图，以模拟概率均值为 0.5(表示混合像元中的海水和陆地类型面积比例各占 50%)的等值线作为海岸线制图结果。以 1m 间隔距离沿目视解译绘制的海岸线创建样点，分别计算各样点到监督分类预测岸线及条件模拟预测岸线之间的最短距离，以此来估算海岸线制图精度。结果表明，到监督分类预测岸线的最短距离均值为 213m，而到条件模拟预测岸线的最短距离均值为 3m。图 6(a)中以高分辨率图像海岸线的目视解译结果为基准的岸线分析显示，相比之应用于原始图像的监督分类预测岸线，应用于 SIcS 图像的条件模拟预测岸线能更精确与现实的表达精细尺度上的海岸线空间分布特征。图 6(b)为 SIcS 图像的模拟概率均值变差函数，与原始数据的低分辨率海水类型组分变差函数模型(图 4(b))比较可见，超分辨率模拟图像可以较好的保持原始数据的空间结构特征。

### 3.6 河口段淤泥质海岸制图结果

对于黄河河口段的淤泥质海岸(图 1 中 B)，采用与黄河海港段海岸相同的研究方法得到超分辨率制图结果，如图 7。海岸线制图精度分析结果表明，目视解译绘制的海岸线上的各采样点到监督分类预测岸线的最短距离均值为 11.7m，到条件模拟预测岸线的最短距离均值为 9.58m，两者相差不大。图 7(a)中以高分辨率图像海岸线的目视解译结果为基准的

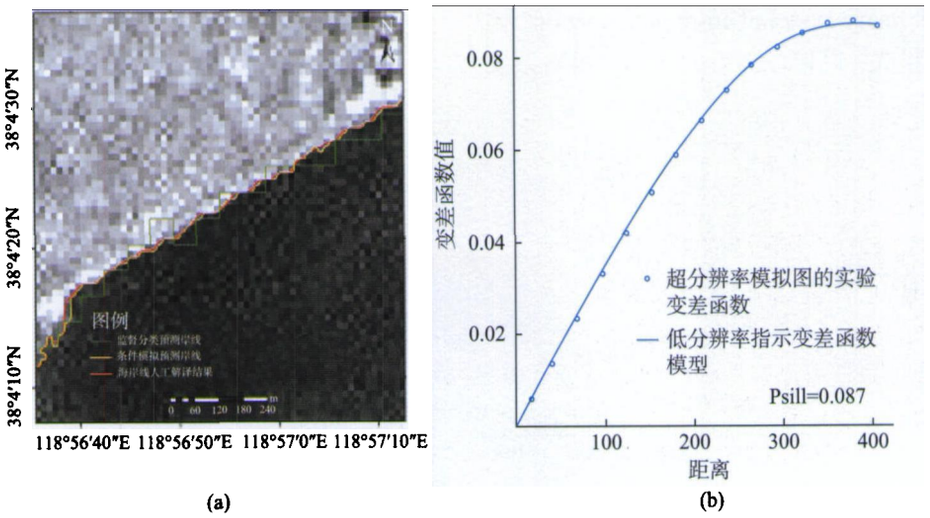


(a) (b)

图 6 (a) 应用于原始图像的监督分类预测岸线与应用于 SIcS 图像的条件模拟预测岸线之间的比较; (b) 由模拟概率均值计算得到的变差函数保持了低分辨率空间结构特征

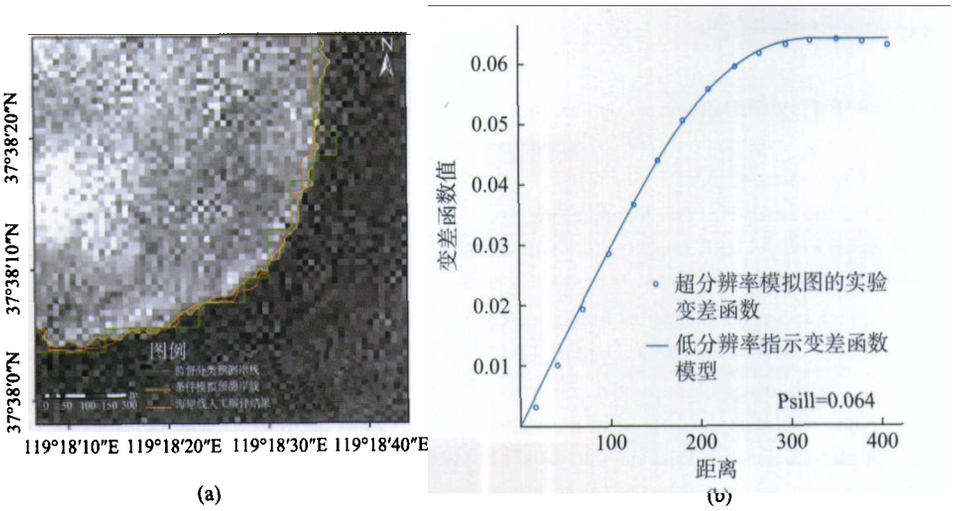


(a)　(b)

图 7　(a) 黄河河口段淤泥质海岸应用于原始图像的监督分类预测岸线与应用于 SIcS 图像的条件模拟预测岸线之间的比较; (b) 由模拟概率均值计算得到的变差函数

岸线分析显示，相比之应用于原始图像的监督分类预测岸线，应用于 SIcS 图像的条件模拟预测岸线能更加现实的表达精细尺度上的海岸线空间分布特征。图 7(b) 中 SIcS 图像的模拟概率均值变差函数的 Psill 值为 0.064，接近于与原始数据的低分辨率海水类型组分变差函数 Psill 值(0.068)。总体来看，图 1 中 B 的淤泥质海岸超分辨率制图精度与图 1 中 A 的直线型人工海岸相比略逊一筹。

## 4　结论与讨论

中国的海岸线总长 3.2 万 km 多，其中大陆海岸线北起鸭绿江口，南至北仑河口，长 1.8 万 km 多(崔乃夫，1998)。因而即使是在高精度遥感数据源日益丰富的今天，使用多种空间分辨率遥感图像进行区域尺度的海岸调查与制图也是必要的。应用于海岸研究的遥感数据主要包括 SAR、近红外、短波红外和热红外图像。其中 SAR 图像的存档数据很少，目前在海岸带还得不到广泛应用。通过被动式光学传感器获取的高空间分辨率卫星图像(比如 IKONOS 和 QuickBird)，以及新近发展起来的 LIDAR 和 InSAR 技术具有获取海岸细部特征信息的能力，但花费昂贵，不适宜在大范围区域应用。相比较，中等空间分辨率图像价格便宜且覆盖范围大，其中 Landsat 卫星图像具有 30 多年的数据记录，尤其适合作为区域尺度上海岸信息提取与变化分析的数据源。本文将超分辨率制图理念引入到基于中等空间分辨率遥感数据的海岸线特征信息提取与制图中，应用克里格与条件模拟等地统计学方法，集成高低分辨率遥感数据的光谱与空间特征信息，以此为基础绘制精细尺度上的海陆环境空间分布特征。试验结果表明，基于协同克里格和条件协同模拟技术生成的海陆类型模拟图像融合了高分辨率变差函数模型所蕴含的先验信息，可以较好的表达精细尺度上的海岸线空间分布特征，同时能够保持原始数据的海陆类型组分值及其空间结构信息。

总之，超分辨率制图技术在空间结构先验模型的基础上，根据当前尺度的数据或信息生成多个模拟实现探寻目标尺度上未知属性值的类型概率分布。其意义并非在于获取某特定地区更为精确的海岸线或其他地表覆盖类型空间分布的超分辨率图像，而是从当前可用的各种尺度与精度信息中探索未知属性在目标尺度的实现，并且这些实现与当前的可用信息相匹配。在这里，制图精度的概念可理解为模拟实现尽可能的准确保持这些可用信息及其空间结构特征。超分辨率图像可以作为输入数据服务于更加细致的空间分析环境、耦合环境模型或决策支持系统，为探索上述模型的输出结果由于缺乏合适分辨率信息产生的不确定性提供不确定性扩散与分析的技术框架 (Boucher & Kyriakidis, 2006)。通过海岸线超分辨率制图研究，地统计学方法使用变差函数结构模型集成多尺度乃至多源空间数据和信息的潜力也得到了展示。本文的研究对象属于较为简单的人工海岸和自然淤泥质岸类型，对于诸如长江口、杭州湾这些区域高浊度背景下的海岸线超分辨率提取研究，构建高质量的复杂环境下的空间结构先验模型尤为重要，可以在空间结构先验模型的推导过程中融合地面调查资料和专家知识等其他多种类型信息。此外，新近发展的多点地统计学理论采用训练图像替代变差函数，有望克服二点地统计学在表达复杂空间结构及再现目标几何形态方面的不足(Boucher 等, 2008)。

## REFERENCES


Atkinson P M and Curran P J. 1995. Defining an optimal size of support for remote-sensing investigations. *IEEE Transactions on Geoscience and Remote Sensing*, **33**(3): 768—776

Atkinson P M, Cutler M E J and Lewis H. 1997. Mapping sub-pixel proportional land cover with AVHRR imagery. *International Journal of Remote Sensing*, **18**(4): 917—935

Atkinson P M. 1997. Mapping sub-pixel boundaries from remotely sensed images. Kemp Z. Innovations in GIS 4. London: Taylor and Francis

Atkinson P M. 2004. Super-resolution land cover classification using two-point histogram. X Sanchez-Villa and Carrera J G H J. GeoENV IV Geostatistics for Environmental Applications, New York: Springer-Verlag

Boak E H and Turner I L. 2005. Shoreline definition and detection: a review. *Journal of Coastal Research*, **21**(4): 688—703

Boucher A and Kyriakidis P C. 2006. Super-resolution land cover mapping with indicator geostatistics. *Remote Sensing of Environment*, **104**(3): 264—282

Boucher A, Kyriakidis P C and Cronkite-Ratcliff C. 2008. Geostatistical solutions for super-resolution land cover mapping, *IEEE Transactions on geosciences and remote sensing*, **46**(1): 272—283

Carle S F and Fogg G E. 1996. Transition probability-based indicator geostatistics. *Mathematical Geology*, **28**(4): 453—476

Carr J R, Bailey R E and Deng E D. 1985. Use of indicator variograms for an enhanced spatial analysis. *Mathmatical Geology*, **17**(8): 797—811

Chappell A, Seqquist J W and Eklundh L. 2001. Improving the estimation of noise from NOAA AVHRR NDVI for Africa using geostatistics, *International Journal of Remote Sensing*, **22**: 1067—1080

Chen S L, Zhang G A and Gu G C. 2004. Mechanism of heavy coastal erosion on Yellow River Delta and its countermeasures. *Journal of Hydraulic Engineering*, **7**: 1—7, 16

Chilès J P and Delfiner P. 1999. Geostatistics: modeling spatial uncertainy. New-York: Wiley Inter-Science

Cui N F. 1998. The Gazetteer of the People's Republic of China: vol 1. Beijing: The Commercial Press

Foody G M, Muslim A M and Atkinson P M. 2005. Super-resolution mapping of the waterline from remotely sensed data. *International Journal of Remote Sensing*, **24**: 5381—5392

Foody G M. 1996. Approaches for the production and evaluation of fuzzy land cover classifications from remotely sensed data. *International Journal of Remote Sensing*, **17**: 1317—1340

Frazier P S and Page K J. 2000. Water body detection and delineation with Landsat TM data. *Photogrammetric Engineering and Remote Sensing*, **66**(12): 1461—1467

Garrigues S, Allard D, Baret F and Weiss M. 2006. Quantifying spatial heterogeneity at the landscape scale using variogram models. *Remote Sensing of Environment*, **103**: 81—96

Goovaerts P. 1997. Geostatistics for Natural Resources Evaluation. New York: Oxford University Press

Gringarten E and Deutsch CV. 2001. Variogram interpretation and modeling. *Mathematical Geology*, **33**(4): 507—534

Journel A G and Alabert F. 1989. Non-Gaussian data expansion in the earth sciences. *Terra Nova*, **1**(2): 123—134

Journel A G and Huijbregts C J. 1978. Mining Geostatistics. San Diego: Academic Press

Journel A G. 1983. Nonparametric estimation of spatial distributions. *Mathematical Geology*, **15**(3): 445—468

Malthus T J and Mumby P J. 2003. Remote sensing of the coastal zone: an overview and priorities for future research. *International Journal of Remote Sensing*, **24**: 2805—2815

Manavalan P, Sathyanath P and Rajegowda G L. 1993. Digital image analysis techniques to estimate waterspread for capacity evaluations of reservoirs. *Photogrammetric Engineering and Remote Sensing*, **59**(9): 1389—1395

Muslim A M, Foody G M and Atkinson P M. 2007. Shoreline mapping from coarse-spatial resolution remote sensing imagery of Seberang Takir, Malaysia. *Journal of Coastal Research*, **23**(6): 1399—1408

Ryu J H, Won J S and Min K D. 2002. Waterline extraction from Landsat TM data in a tidal flat: a case study in Gomso Bay, Korea, *Remote Sensing of Environment*, **83**: 442—456

Shen F, Gao A, Wu J P, Zhou Y X and Zhang J. 2008. A Remotely sensed approach on waterline extraction of silty tidal flat for DEM construction, a case study in Jiuduansha Shoal of Yangtze River, Acta Geodaetica et Cartographica Sinica, **37**(1): 102—107

Southworth J. 2004. An assessment of Landsat TM Band 6 thermal data for analyzing land cover in tropical dry forests. *International Journal of Remote Sensing*, **25**(4): 689—706

Tatem A J, Lewis H G, Atkinson P M and Nixon M S. 2003. Increasing the spatial resolution of agricultural land cover maps using a Hopfield neural network. *International Journal of Geographical Information Science*, **17**(7): 647—672

Verhoeye R and De Wulf J. 2002. Land cover mapping at sub-pixel scales using linear optimization techniques. *Remote Sensing of Environment*, **79**(1): 96—104

Zhang Y and Chen S L. 2009. Remote sensing analysis of spatial-temporal pattern on coastline change: a case study in the abandoned Yellow River Delta Coast. *Advances in Marine Science*, **27**(2): 166—175


## 附中文参考文献


陈沈良, 张国安, 谷国传. 2004. 黄河三角洲海岸强侵蚀机理及治理对策. 水利学报, **7**: 1—7, 16

崔乃夫. 1998. 中华人民共和国地名大词典: 第1卷, 北京: 商务印书馆

沈芳, 郜昂, 吴建平, 周云轩, 张杰. 2008. 淤泥质潮滩水边线提取的遥感研究及DEM构建. 测绘学报, **37**(1): 102—107

张旸, 陈沈良. 2009. 苏北废黄河三角洲海岸时空演变遥感分析. 海洋科学进展, **27**(2): 166—175